New Hyperpolarized Carbon-13 MR Markers of Metabolism– Spin-Relaxation, Diffusion, and Kinetic Parameters

Christine Leon[1,2], Peder Larson[1], Adam Kerr[3], Klaus Kruttwig[4], Cornelius Von Morze[1], Simon Hu[1], Robert Bok[1], Andrei Goga[4], John Pauly[3], Sarah Nelson[1,2], John Kurhanewicz[1,2], Daniel Vigneron[1,2]

[1]Department of Radiology and Biomedical Imaging, University of California, San Francisco, [2]UC Berkeley-UCSF Graduate Program in Bioengineering, [3]Department of Electrical Engineering, Stanford University, and [4]Department of Hematology and Oncology, University of California, San Francisco

Introduction: Magnetic resonance spectroscopy (MRS) of hyperpolarized substrates provides a powerful tool to investigate tissue metabolism and potentially kinetics *in vivo*[1]. However, the accuracy of current methods to calculate kinetic parameters and T_1 relaxation effects have been limited by extracellular signal contributions, complex models, and reduced precision at lower SNR[2]. To address these challenges, we investigated a new modeling technique using Metabolic Activity Decomposition (MAD) and stimulated echo acquisition mode (STEAM) which separates exchanging from non-exchanging metabolites providing twice the information as conventional techniques[3,4]. This allows for accurate measurements of multiple rates of conversion, apparent diffusion coefficients (ADC) and T_1s values simultaneously, providing further biological information about the cellular environment of the metabolites.

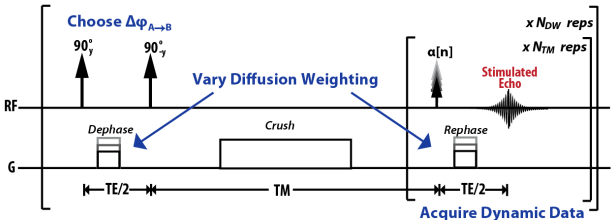

Figure 1. Dynamic MAD-STEAM pulse sequence with varying diffusion weighting.. All data was acquired with slab selection in z, 20x, 1sec temporal resolution, 256 spectral points, 2.5 kHz spectral bandwidth, progressive flip angle, and adiabatic double spin echo.[5]

Methods: STEAM in the presence of metabolic conversion creates a phase shift dependent on the resonance frequency and echo time (TE), $\Delta\varphi = 2\pi fTE/2$.[3] By choosing $\Delta\varphi = \pi/2$, the spins generated during a mixing time (TM), can then be separated during reconstruction.[3] Co-polarization with ^{13}C-urea was used as a phase reference.[3] $T_{1,Eff}$ and $K_{Pyr\to x}$ are calculated using MAD.[7] Since the $S(t) \propto e^{-t/T_1} e^{-bD}$, the ADCs and T_1s were can be calculated by $ADC = \frac{\Delta(1/T_{1,Eff})}{\Delta(\vec{G}^2)(\gamma\delta)^2\left(\frac{\delta}{3}\right)}$ and $1/T_1 = 1/T_{1,Eff,i} - (\vec{G}_i)^2(\gamma\delta)^2\left(\frac{\delta}{3}\right)ADC$.

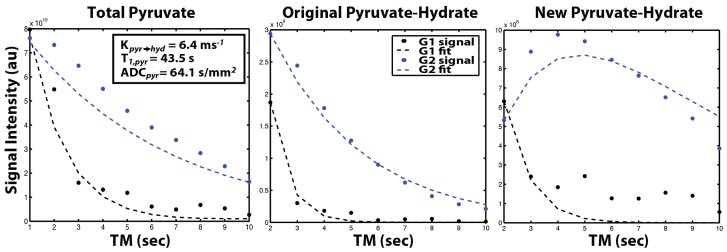

Figure 2. Total Pyruvate, Orginal Pyrvuate-Hydrate and New Pyrvuate-Hydrate dynamic curves from a MAD-STEAM sequence (G1 = 3.04s/mm^2 and G2=1.14s/mm^2.

Results & Discussion: In addition to significantly higher to $K_{Pyr\to Lac}$ in tumors using MAD, the $T_{1,Eff}$ of lactate was shorter in tumors suggesting a different cellular environment of lactate. The measurement of $T_{1,Eff}$ is a combination of both relaxation and diffusion effects which can be separated using the pulse sequence shown in Figure 1. In the liver where there is high conversion to alanine, a three-site exchange model was used (Figure 3). $K_{Pyr\to Lac}$ measured with MAD (R^2 = 0.809) demonstrated a higher correlation with LDH activity than modeling with magnitude of the data (R^2 = 0.343). $K_{Pyr\to Lac}$ measured with MAD also had a higher correlation than metabolite ratios such as the lactate-to-pyruvate ratio (R^2 = 0.662). In a transgenic model of oncogene-driven liver cancer, changes in $K_{Pyr\to Ala}$ can be observed between baseline, two weeks (pre-tumor) and two months (late tumor) off doxy (Figure 4). This demonstrates that the $K_{Pyr\to Ala}$, may also be a valuable in addition to $K_{Pyr\to Lac}$ in the understanding of the metabolism of disease, particularly in cancer formation in the liver.

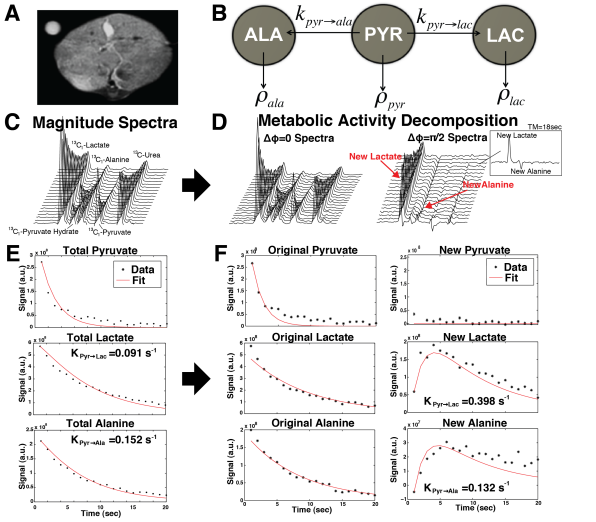

Figure 3. **(a)** T_2W axial anatomical image in slab. **(b)** Three-site exchange system. Stacked plots of the successively acquired **(c)** magnitude, **(d)** real ($\Delta\varphi$=0) and imaginary ($\Delta\varphi$=π/2) spectra. Peak areas from **(e)** the magnitude spectra with

Conclusion: With the removal of confounding signals from the vasculature, improved accuracy of estimation of real-time conversion rates, and simultaneous measurement of ADCs and T_1s, the developed technique provides new and more accurate quantitative measures of relaxation, diffusion, and conversion rates. This technique has great biomedical potential as it could be used to better measure tumor metabolic changes with carcinogenesis, progression and response to therapy.

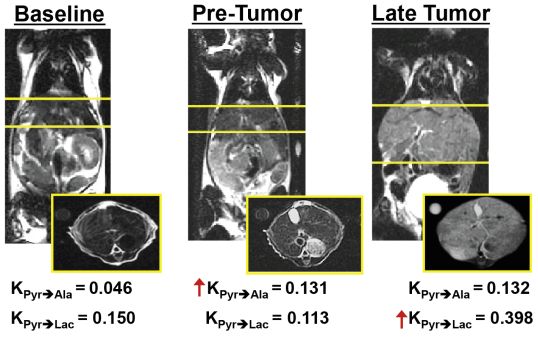

Figure 4: T_2-W anatomical images showing progression in a switchable oncogene driven model of liver cancer and the corresponding parameters using MAD-STEAM: baseline, two weeks (pre-tumor) and two months (late tumor) off doxy.

References: [1] Kurhanewicz, et al. Neoplasia. 2011; 13(2): 81-97. [2] Santarelli, et al. NMR in Biomed 2011; 25(7):925-934. [3] Larson, et al. Proc Intl Soc Mag Reson Med 19, #655 (2011). [4] Larson et al. IEE Trans Med Imaging, 2011; 31:265-275. [5] Cunningham, et al. J Magn Reson 2007; 187:357-362. [6] Goga, et al. Nature Med 2007;13:820-827. [7] Leon, et al. Proc Intl Soc Mag Reson Med 20, #180 (2012).

Acknowledgements: The authors acknowledge: Galen Reed, Peter Shin, Lucas Carvajal, Sukumar Subramaniam, and Mark Van Criekinge for assistance performing experiments, as well as Dr. Michael Lustig and Dr. Murat Arcak for their expertise and Dr. James Tropp for the ^{1}H/^{13}C mouse coil, as well as, funding from NIH P41-EB01359, National Science Foundation Graduate Research Fellowship, and NIH K99 EB012064.

Evaluating Tumor Perfusion with Hyperpolarized HP001 and Comparison with Dynamic Susceptibility Contrast MR Imaging and Pathology Using Orthotopic Human GBM Xenografts

Ilwoo Park[1], Cornelius von Morze[1], Jan H. Ardenkjaer-Larsen[2], Janine M. Lupo[1], Motokazu Ito[3], Joydeep Mukherjee[3], Joanna J. Phillips[3], Russell O. Pieper[3], Daniel B. Vigneron[1], Sarah J. Nelson[1]

[1]Surbeck Laboratory of Advanced Imaging, Department of Radiology and Biomedical Imaging, UCSF [2]GE Healthcare, Broendby, Denmark, [3]Brain Tumor Research Center, Department of Neurological Surgery, UCSF

Introduction: Measures of blood vessel volume and permeability in glioblastoma multiforme (GBM) are beneficial for evaluating heterogeneous tumor vasculature and predicting response to therapy [1]. The use of hyperpolarized HP001 (*bis*-1,1-(hydroxymethyl)-[1-^{13}C]cyclopropane-d8) can produce perfusion data with high sensitivity. The purpose of this study was threefold: (i) to characterize tumor perfusion with dynamic ^{13}C HP001 imaging using an orthotopic human GBM xenograft model, (ii) to correlate HP001 data with conventional Gd-based dynamic susceptibility contrast (DSC) imaging data, and (iii) to compare the result from HP001 imaging with immunohistochemistry.

Methods: Ten rats with an orthotopic GBM model were included in this study [2]. Following a polarization of a 50 μL HP001, trityl radical and 1.5 mM Dotarem for ~1 hr using a Hypersense® DNP system and a dissolution with ~5.6 mL heated 1X phosphate buffered saline, 2.7 ml of HP001 solution (100 mM) was injected into the tail vein of the rat. Using a GE 3T scanner with a custom ^{1}H/^{13}C RF coil, dynamic imaging data was acquired every second for 90s using a custom single-slice balanced steady state free precession (bSSFP) pulse sequence [3]. DSC imaging was performed every second for 150s during a second injection of 0.2 mmol/kg Gd-DTPA using a gradient echo, echo planar imaging sequence [4]. HP001 dynamic data (Fig 1a) were characterized in tumor, normal brain and vascular region (Fig 1b) and compared with DSC data from the ΔR2* curve (Fig 1c) and anti-α smooth muscle actin (α-SMA) antibody used to stain for vascular smooth muscle cells.

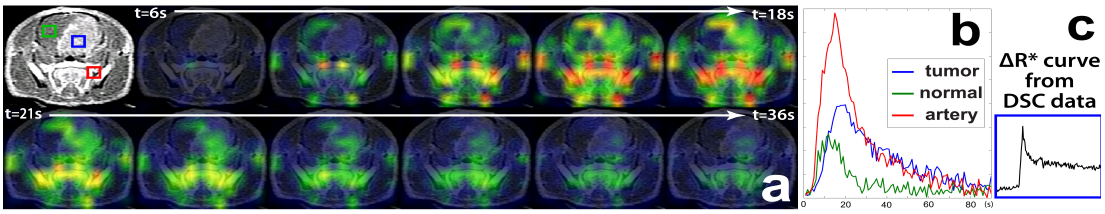

Figure 1. (a) A post-Gd image showing tumor (blue), normal tissue (green), and artery (red) along with dynamic HP001 data displayed every 3s. (b) HP001 signal curves from the corresponding regions. (c) ΔR* curve for the corresponding tumor voxel.

Results: Distinct HP001 characteristics were found between tumor and normal tissues. Tumor exhibited significantly higher mean normalized maximum peak (nMP=0.30±0.11) and mean normalized area under the curve (nAU=0.36±0.16) than normal tissue (mean nMP=0.24±0.06, mean nAU=0.24±0.06) (Fig 2). HP001 signal in normal tissue reached maximum 2s (±2s) prior to maximum signal in the artery and HP001 signal in tumor peaked at 2s (±2s) from the maximum peak in the artery (Fig 2). The tumor perfusion data obtained from hyperpolarized HP001 imaging was strongly correlated with the conventional DSC imaging data (Fig 3) and consistent with the findings from immunohistochemical analysis (Fig 4).

References: [1] Essock-Burn et al., *Neuro Oncol*, 2011 [2] Park et al., *J Magn Reson Imaging*. 2011 [3] Von Morze et al., *J Magn Reson Imaging*. 2011 [4] Lupo et al., *AJNR*, 2005

Acknowledgements: American Brain Tumor Association, a NIBIB supported grant P41EB013598, ITL-BIO04-10148.

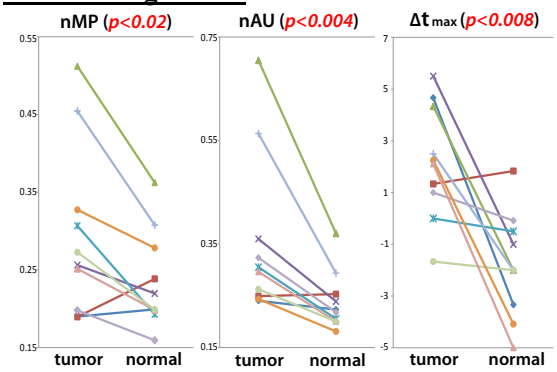

Figure 2. Comparison of HP001 characteristics between tumor and normal tissue. Normalized maximum peak (nMP), normalized area under the curve (nAU) and time from maximum peak to maximum artery peak (Δt_{max}) were significantly different between the two tissue types.

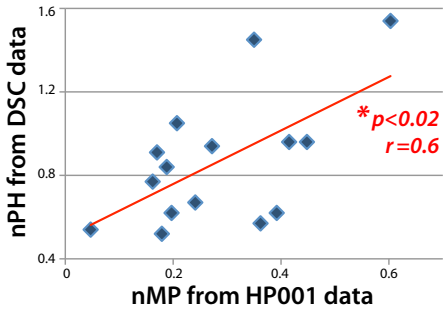

Figure 3. Correlation of normalized maximum peak (nMP) from HP001 data and normalized peak height (nPH) from DSC data

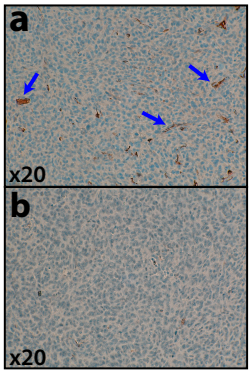

Figure 4. α-smooth muscle actin slides. The rat with a large amount of positive staining (a) had higher nMP and nAU values than the one with little positive staining (b).

High resolution diffusion-weighted imaging to evaluate breast tumor-stromal boundary in patients receiving neoadjuvant chemotherapy

McLaughlin RL[1], Newitt DC[2], Wilmes LJ[2], Proctor E[2], Wisner DJ[2], Jones EF[2], Kornak J[3], Joe BN[2], and Hylton NM[1,2]
[1]The UC Berkeley - UCSF Graduate Program in Bioengineering, San Francisco and Berkeley, California
[2]UCSF Department of Radiology and Biomedical Imaging, San Francisco, California
[3]UCSF Department of Epidemiology and Biostatistics, San Francisco, California

Background: The architecture of the extracellular matrix (ECM) at the breast tumor-stroma border may facilitate tumor invasion. Cancer associated ECM remodeling alters stromal properties and results in increased tissue stiffness, as do alterations in cross-linking, increased collagen deposition, and fiber reorganization. Water movement measured by diffusion-weighted imaging may reflect the ECM remodeling and collagen alignment at the tumor-stroma border, as well as changes in these microstructures in response to treatment. Recently reported results implemented a high-resolution diffusion-weighted imaging (HR-DWI) acquisition with substantially increased in spatial resolution compared to standard breast DWI. We hypothesized that HR-DWI could probe diffusion changes (such as apparent diffusion coefficient, ADC) in tumor and adjacent stromal tissue, providing new quantitative markers for improving the prediction of breast cancer treatment response. Here in, we reported the ADC changes in breast tumors and adjacent stroma in response to neoadjuvant chemotherapy.

Materials and Methods: Seven patients with pathologically confirmed invasive breast cancer were imaged with HR-DWI before treatment (V1) and 3 weeks after the start of taxane-based treatment (V2). The mean ADC was plotted in 1 mm increments around the tumor boundary. The early change in ADC, defined as the change from V1 to V2, was measured for tumor, tumor boundary, and stromal regions, and the relationship to treatment response – defined as post-treatment tumor volume response – was evaluated.

Results: The early change in ADC of tumor and boundary regions had a significantly positive correlation with treatment response (Table I). There is also evidence that the early change in ADC of stroma may correlate with treatment response. In this population, we were unable to determine any relationship between the early change in volume and treatment response.

Conclusions: Our preliminary studies show that early ADC changes in tumor and boundary regions correlate significantly to treatment response, and further data may prove early ADC changes have predictive value for treatment response. The proximity-dependent evaluation of HR-DWI data in both the tumor and adjacent stromal tissue is a novel and potentially powerful technique for evaluating patient response to therapy.

Table I. The p values of the Spearman rank correlation between treatment response and ADC measurements

		V1 to V2		
	Region (mm)	ρ	95% CI	p value
ADC_{prox}	2 to 5	0.14	-0.684 to 0.809	0.76
ADC_{dist}	9 to 13	0.714	-0.084 to 0.954	0.07
ADC_{inner}	-5 to -2	0.750	-0.007 to 0.961	0.05
$ADC_{wholetumor}$	-∞ to 0	0.929	0.584 to 0.990	0.003
ADC_{bound}	-2 to 2	0.857	0.294 to 0.979	0.01
$ADC_{tumor+bound}$	-∞ to 2	0.929	0.584 to 0.990	0.003

Each ADC variable represents the respective region indicated relative to the tumor border. V1 and V2 are used to indicate visits 1 and 2. ρ is the estimated Spearman correlation. 95% CI indicates the 95% confidence interval.

Predicting Disease Progression With Multiparametric Magnetic Resonance Imaging in Patients With Prostate Cancer Managed by Active Surveillance

Robert R. Flavell, Carmin J. Liang, Antonio C. Westphalen, John Kurhanewicz

Abstract: Prostate cancer is the most prevalent noncutaneous cancer, and responsible for the second most cancer-related deaths in men. There is a broad clinical spectrum of prostate cancer, with some patients presenting with indolent disease, while others present with a rapidly progressive, fatal course. At present, treatment selection is based on three principal factors: histology (Gleason scoring), prostate specific antigen (PSA) level, and clinical staging. Those with low risk disease may elect to be managed with active surveillance, which relies on serial PSA measurements, biopsy, and clinical exam for evaluation of progression to more aggressive disease.

Prostate magnetic resonance imaging (MRI) has an adjunct role in the management of prostate cancer in general and active surveillance patients in particular. A typical prostate MRI performed at UCSF incorporates multiple sequences, including T1 and T2 weighted imaging, and apparent diffusion coefficient (ADC) map for evaluation of local metastasis and presence of suspicious prostate nodules, and magnetic resonance spectroscopy (MRS) to identify abnormal metabolism. In many cases aggressive disease can be identified and then subsequently treated. However, the relative contribution of these different sequences, and their ability to predict disease progression in active surveillance patients remains unclear.

We present a retrospective study evaluating a cohort of 119 prostate cancer patients managed by active surveillance, who were evaluated by multiparametric MRI. Mean follow up time post MRI imaging was 43 months. Of the 119 patients, 59 progressed based on either upgrade of Gleason score on subsequent biopsy, rapid PSA velocity (greater than 0.75 μg/L/yr), or progression to definitive treatment. Imaging was evaluated based on three parameters: presence of a T2 dark nodule, quantitative evaluation of ADC measurements of suspicious nodules, and detection of 3 or more consecutive voxels of suspicious MRS signal (defined as a choline plus creatine to citrate ratio greater than two standard deviations above the normal value).

Individually, no single technique, or pairwise combination of two techniques, was able to predict disease progression in a statistically significant manner. Importantly, the combination of all three techniques was able to predict disease progression with an odds ratio of 2.91 (95% confidence interval of 1.19 – 7.08). Similarly, lack of concordant positive result on all 3 techniques yielded an odds ratio for no progression of 2.84 (95% confidence interval of 1.26 – 6.37). Receiver operator curve (ROC) analysis for all three modalities, using a regression model and bootstrapping, demonstrated a combined area under the ROC curve of 0.65. Overall, these preliminary data indicate that multiparametric analysis, including T2 weighted imaging, MRS, and ADC, is essential to maximizing predictive value of prostate cancer MRI. Furthermore, MRI could play an important role in selecting patients on active surveillance who may be optimal for ongoing surveillance, versus those who are likely to progress and will need definitive treatment.

Longitudinal Comparison of Metabolite ratios in Neonates with Hypoxic Ischemic Encephalopathy.

Lee PL[1], Tymofiyeva O[1], Ferriero DM[2], Barkovich AJ[1], Xu D[1,3]
Department of Radiology, Department of Pediatrics and Neurology, Joint UCSF/UC Berkeley Graduate Group in Bioengineering

Purpose

Proton MR Spectroscopy (1H-MRS) is a valuable tool for studying neurodevelopment in infants with Hypoxic Ischemic Encephalopathy (HIE). Studies have illustrated prognostic value in determining ratios between Lactate (Lac), N-acetyl aspartate (NAA), and Choline (CHO) from newborn infants[1]. We studied neonates with signs of HIE by looking at the metabolite ratio differences between infants with abnormal and normal outcome at approximately 4 days of life and at 6 months. A longitudinal comparison was also performed to determine changes in metabolite ratio across outcome groups.

Materials & Methods

A comprehensive MRI exam with lactated edited 3D MRS was performed at approximately 4 days and at 6 months of life for 25 newborns with HIE using methods previously described [2]. All subjects were examined by a pediatric neurologist at 6 months of age and were neurologically evaluated using a Neuromotor Scoring system validated at our institution[3]. Nine patients had Abnormal neurologic outcome (NMS≥2), and 16 patients had Normal outcome (NMS≤1).

The MRS data was sent to an off-line Sun Workstation (Sun Microsystems, Mountain View, Ca) for post-processing quantification and analysis. A basal ganglia (BG) region of interest (ROI) was drawn bilaterally on T2 images, in which spectroscopic data were collected[4]. Left and right ROIs were found to be statistically similar and were combined for analysis. Linear Regression with age corrections was performed for statistical comparison.

Results

Infants in the Abnormal cohort had statistically higher CHO/NAA ratios at term and a statistically higher LAC/NAA at the 6 month time point, in comparison to the Normal outcome group. Both Normal and Abnormal outcome groups had a decrease in CHO/NAA and LAC/NAA ratios over time, suggesting increases in NAA as the brain matures despite the hypoxic insult. The Abnormal outcome group shows a higher degree of change over time, though not statistically significant.. (Table 1)

Table 1 LSMean	At Term			6 Months			Change		
	Normal	Abnormal	P-Value	Normal	Abnormal	P-Value	Normal	Abnormal	P-Value
CHO/NAA	1.77	2.07	0.0136*	1.06	1.11	0.6123	-0.68	-0.90	0.0876
LAC/NAA	0.13	0.18	0.2800	0.05	0.07	0.0473*	-0.08	-0.12	0.4251
LAC/CHO	0.08	0.09	0.4865	0.05	0.06	0.3213	-0.03	-0.02	0.8034

*Statistically significant at the 5% level
**Change=(Mean Scan2-Mean Scan1)

Conclusion

The study has confirmed previous findings that HIE patients with worse outcome have substantial lactate levels and higher CHO/NAA ratios resulting from cellular breakdown and damage[5]. This pattern persists after 6 months, which may indicate that the effects are long lasting and the patients are still recovering from injury. Due to the small number of patients included in this study, this pattern must be confirmed in a larger cohort that could point to needs for further treatment during management of these patients.

Locally Linear Embedding (LLE) for MRI based Alzheimer's Disease Classification

Xin Liu, Duygu Tosun, Michael W. Weiner, and Norbert Schuff

Magnetic resonance imaging (MRI) measurements of brain atrophy in Alzheimer's disease (AD) are increasingly processed using modern machine learning algorithms for pattern recognition to identify individuals with early signs of the disease. So far, however, a reliable diagnosis for AD based on MRI has not been successful, partially because brain features are highly complex.

We report a successful application to improve AD classifications by reducing effectively the high dimensionality of brain features. Specifically, we used locally linear embedding (LLE), an unsupervised statistical learning method to map nonlinearly high dimensional features of brain regional volume and cortical thickness onto a linear space of a few dimensions. Then, we perform AD classifications in the LLE embedded features. We tested the approach on 414 subjects from the Alzheimer's disease neuroimaging initiative (ADNI) who had three or more consecutive MRI scans over 3 years and also had one of the following clinical diagnoses: stable cognitive normal (CN; n=138), stable mild cognitive impairment (s-MCI; n=93), MCI conversion to AD (c-MCI; n=97), and AD (n=86). LLE computes low-dimensional, local feature preserving embeddings while maintaining the ability to learn the global structure of nonlinear manifolds, e.g. variations in regional volumes across all brain regions. Fig. 1 illustrates the performance of LLE dimension reduction from 162 (68 features are cortical thickness and 94 features are regional volume) spanned by the brain regions to two embedded dimensions. The strikingly distinct clustering of the groups (CN = dark blue, s-MCI = cyan, c-MCI = yellow, and AD = red) in the two dimensional embedded space, indicating that LLE learned the global features of brain atrophy in each group effectively while preserving these features in an embedded space of only 2 dimensions.

Furthermore, we applied three state-of-the-art classification algorithms to perform pair wise classification on this data. We found classifications using embedded features of regional volume and cortical thickness generally outperformed ($p<0.001$) classifications that used the original features directly. Moreover, the benefit of LLE was largely independent of the classifier algorithms. We obtained similarly AD classification performance by regularized logistic regressions with elastic net (EN), support vector machine (SVM), and linear discriminant analysis (LDA). Most strikingly, classifications using the embedded features reliably separated among MCI individuals those who converted to AD and those who did not convert (accuracy = 0.69). In contrast, the same classifications using the original brain features performed not better than chance (accuracy = 0.58). Receiver operating characteristic (ROC) curves are for AD vs. CN, and s-MCI vs. c-MCI classifications are provided in Fig. 2.

In conclusion, high-dimensional classifications using brain MRI data should use LLE to reduce dimensionality. The improvement in identifying among individuals with MCI those who convert to AD could have important implications for conversion prediction, early diagnosis, and therapeutic trails of AD that target preclinical intervention.

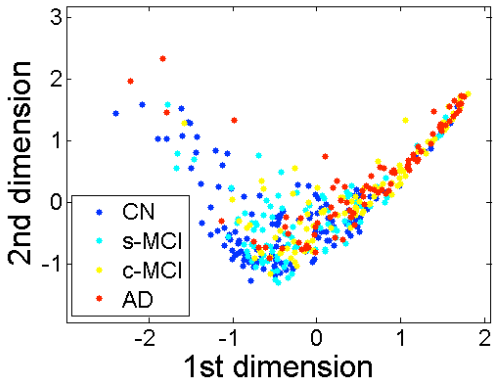

Fig. 1. Visualization of 414 subjects in 2-D LLE space based on 98 brain regional volume features and 68 cortical thickness features.

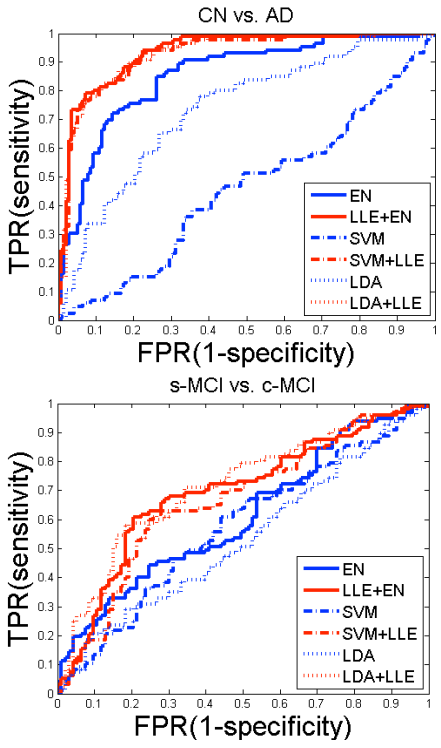

Fig. 2. ROC curves of pair wise classifications using different classifiers: EN, SVM, and LDA with and without LLE.

Hemodynamic Imaging Biomarkers of Progressive Aortic Disease

S. Jarrett Wrenn, MD PhD; Monica Sigovan, PhD; Petter Dyverfeldt, PhD; David Saloner, PhD; and Michael D. Hope, MD

PURPOSE Bicuspid aortic valve (BAV) is a common anomaly and is associated with ascending aortic dilation, causing significant morbidity and mortality. The pathophysiology of this association is unclear, but 3D cine MR flow imaging (4D Flow) has revealed unique systolic helical flow. Several quantitative hemodynamic imaging parameters can be derived from 4D Flow and might underlie and thus predict progression of aortic pathology in BAV. We investigate the relationships between aortic growth and flow eccentricity, peak velocity, normalized flow displacement, and aortic wall shear stress (WSS). The reproducibility of these 4D Flow derived hemodynamic parameters is also evaluated.

MATERIALS AND METHODS Serial CTA or MRAs were reviewed in 25 patients evaluated by 4D Flow, including 13 BAV and 12 controls. Ascending aortic measurements were made at standard levels by two reviewers, and growth rates of maximally enlarged segments were determined. Using described methods, AsAo flow eccentricity was graded for all patients. Two observers independently calculated the following hemodynamic parameters from 4D Flow data: peak velocity, normalized flow displacement, maximum WSS, minimum WSS, and mean WSS. Reproducibility analysis was performed for these parameters. Growth rates were compared between BAV and control groups, and within the BAV group based upon eccentricity. Growth rates were also correlated with the calculated hemodynamic parameters.

RESULTS Average follow-up was 4.3±2.9 y. Growth rates were higher in the BAV group ($p<0.01$). BAVs with eccentric flow showed higher growth rates than those with normal flow (1.0 vs 0.1mm/y, $p=0.02$), and those with marked eccentricity exhibited more rapid growth than other BAV patients (1.2 vs 0.3mm/y, $p=0.02$). Normalized displacement and peak velocity were very reproducible and showed good ($r=0.65$) and moderate ($r=0.35$) correlation with growth, respectively. WSS parameters were fairly reproducible but correlated poorly with growth.

CONCLUSION We demonstrate that aortic growth is linked to abnormal hemodynamics in patients with BAV. Higher growth rates are seen with increased flow eccentricity. Normalized flow displacement is a simple and reproducible 4D Flow derived parameter that correlates well with aortic growth in our cohort. WSS estimated by MRI, however, does not correlate well. Our results suggest that MR blood flow imaging may become central for risk stratifying the 1-2% of the population with BAV. Evaluation of hemodynamics – specifically normalized displacement –could potentially be used to guide imaging surveillance intervals and early intervention.

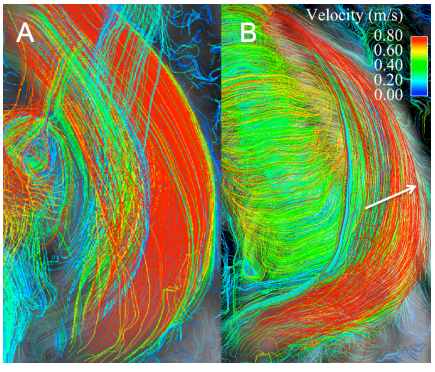

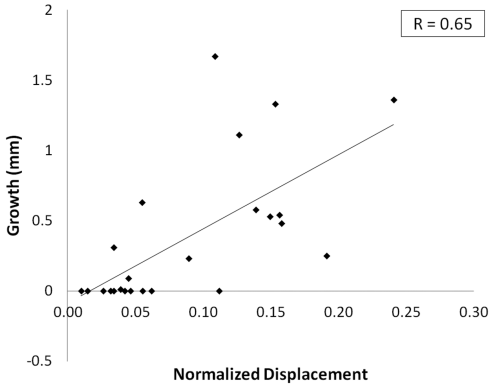

Low unsaturated bone marrow lipids as a novel imaging biomarker in postmenopausal women with prevalent fragility fractures

Janina M. Patsch[1], Xioajuan Li[1], Thomas Baum[1], Samuel P. Yap[1], Dimitrios Karampinos[1], Ann V. Schwartz[2], Thomas M. Link[1]

[1] MQIR, Department of Radiology & Biomedical Imaging, UCSF
[2] Department of Epidemiology and Biostatistics, UCSF

Background: MR-spectroscopy provides a non-invasive option for the quantification of bone marrow fat content and bone marrow fat composition. Both of these parameters have been linked with poor bone quality and type-2 diabetes mellitus, however a dedicated study with diabetic and non-diabetic fracture subjects and corresponding controls has not yet been performed. The goal of this non-invasive MR imaging study was to quantify bone marrow fat content and composition in diabetic and non-diabetic postmenopausal women with prevalent fragility fractures and to compare them with non-fracture controls with and without type-2 diabetes mellitus.

Methods: Sixty-nine postmenopausal women (mean age 63±5 years) were recruited. Thirty-six patients (47.8%) had at least one fragility fracture. Seventeen fracture patients were diabetic. Thirty-three women (52.2%) were non-fracture controls. Sixteen of these women were diabetic non-fracture controls. To quantify the amount of bone marrow fat and its composition, patients underwent MR spectroscopy of the lumbar spine at 3 Tesla (Figure 1). Bone mineral density (BMD) was determined by dual energy X-Ray absorptiometry (DXA) of the hip and lumbar spine and quantitative computed tomography (QCT) of the lumbar spine. In addition blood was drawn to measure fasting glucose, Hba_1c, calcium, PTH, 25-(OH)-vitamin D, and CRP levels.

Results: Total marrow fat content did not differ between fracture (68.3%) versus non-fracture patients (69.9%, p=0.176, adjusted for age and race). However, unsaturated lipids (UL) were significantly lower in patients with than without prevalent fragility fractures (-29.3%, p<0.0001, adjusted for age, race, and spine BMD by QCT; Figure 1A). Likewise, diabetics had lower UL bone marrow lipids than non-diabetics (p<0.0001, adjusted for age, race, and spine BMD by QCT; Figure 1B). Diabetics with fractures (DMFx) had lower UL than diabetics without fractures (DM, p= 0.002; Figure 1C). According to DXA and QCT, healthy controls, diabetic and non-diabetic fracture patients and non-fractured diabetics had osteopenic BMD. Nevertheless, BMD was highest in non-fractured diabetics and lowest in non-diabetic fracture cases. Mean unsaturated lipid levels were correlated with mean BMD of the lumbar spine by QCT (r=0.261, p=0.030) but not by DXA (r=0.087, p=0.483). There were no significant correlations between BMD and total marrow fat. Fasting glucose and Hba_1c levels were significantly higher in diabetics (152.9 mg/dl; 7.7 %) than non-diabetics in whom they were normal (p<0.0001). 25-(OH)-Vitamin D was significantly lower in diabetics than non-diabetics (p=0.034).

Conclusion: The results of this study suggest that low unsaturated bone marrow lipids are linked with prevalent fractures in both diabetics and non-diabetics. Non-invasive quantification of unsaturated bone marrow fat composition by MR-spectroscopy may therefore serve as a novel tool for fracture risk assessment.

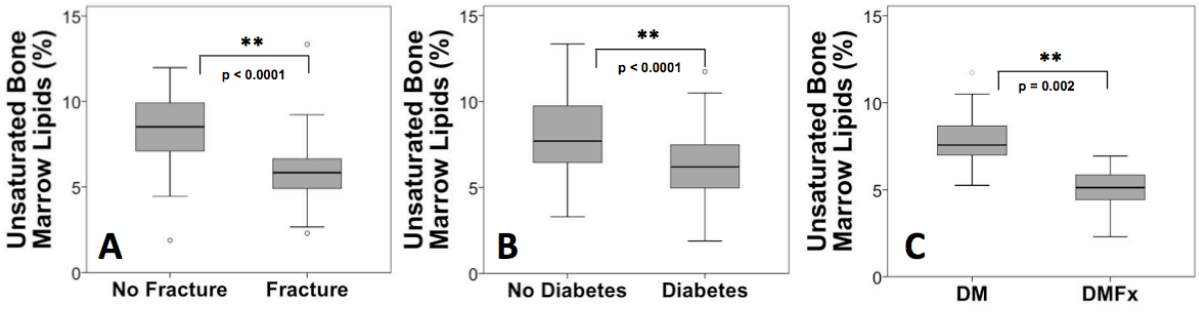

Figure 1. Unsaturated bone marrow lipids. A) Fracture versus non-fracture patients B) Type-2 diabetics versus non-diabetics. C) Diabetics with fracture versus diabetics without fractures

Improving Efficiency of Pulmonary Embolism (PE) Testing In Young Patients

John Mongan, MD, PhD, Jeffrey Kline, MD, Rebecca Smith-Bindman, MD

Purpose:

PE is known to have lower prevalence in younger than older people, and disease often presents differently in different age groups, but prior investigations have looked at PE in the adult population as a whole. We compare the proportion of PE imaging (pulmonary CT angiography and V/Q scan) that results in a positive diagnosis by sex and age. As explanation for age-related differences, we investigate age-specific predictive values of common clinical indicators of PE. We develop a rule to improve testing efficiency by excluding very low risk young patients from PE.

Materials and Methods:

We used the 2009 Nationwide Emergency Department Sample (NEDS) from the Agency for Healthcare Research and Quality (AHRQ) to estimate the number of patients in US emergency departments evaluated for PE and the proportion with positive examinations for PE. Data from the Pulmonary Embolism Research Consortium (PERC, n=7889) were used to compare significance of indicators of PE between young and older adults, and project performance of a clinical decision rule for PE imaging in young patients.

Results:

Table 1 demonstrates strong age- and sex-related trends in proportion of PE-positive imaging, which run opposite to the trends of radiation exposure carcinogenesis risk. Women aged 18-35 were about eight times less likely to have a PE than women over 50 (0.06% vs 0.48%, RR 95% CI 0.12-0.15), yet were imaged only 30% less frequently (2.7% vs 3.8%, RR 95% CI 0.66-0.76), resulting in a far lower proportion of positive exams in young women (2.3% vs 12.3%). Women were also imaged for PE more frequently, with lower proportions of positive studies, than men of the same age. Tachycardia is a significant predictor of PE in older (OR: 1.41-2.11, $p<0.001$), but not younger (OR: 0.65-1.80, $p=0.76$) patients. Conversely, fever is a significant predictor in younger (OR: 1.46-7.38, $p=0.003$), but not older (OR: 0.65-1.04, $p=0.87$) patients. An imaging clinical decision rule based on these differences is projected to avoid 62% of PE imaging in young people, reducing the number needed to test from 23 to 10, with a missed PE rate of 0.9% in those excluded from imaging.

Conclusions:

Despite low rates of PE, young women are imaged for PE almost as frequently as older patients with much higher rates of PE, resulting in an imaging risk/benefit ratio for young women approximately 50 times less favorable than for elderly men. This may be partially due to concern raised by indicators of PE that are not significant in young patients, such as tachycardia. Limiting PE imaging to young patients with at least one significant indicator of PE is projected to more than halve the number of young people imaged for PE while continuing to identify more than 99% of the PEs diagnosed with current scanning practices.

	Male			Female		
Age	PE	Imaged	PE+ Imaging	PE	Imaged	PE+ Imaging
18-35	8.8±0.3 (0.06%)	216.3±5.0 (1.5%)	4.0±0.1%	13.9±0.6 (0.06%)	602.1±12.4 (2.7%)	2.3±0.1%
36-50	23.3±0.8 (0.21%)	310.3±6.9 (2.8%)	7.5±0.2%	24.1±0.8 (0.18%)	590.7±12.0 (4.3%)	4.1±0.1%
51-65	37.4±1.2 (0.43%)	277.2±5.9 (3.2%)	13.4±0.3%	31.8±1.0 (0.32%)	436.5±9.2 (4.5%)	7.3±0.2%
>65	51.5±1.6 (0.61%)	238.0±5.3 (2.8%)	21.4±0.4%	73.1±2.2 (0.60%)	417.1±8.9 (3.4%)	17.4±0.4%

Table 1:
Number (in thousands) and standard errors of PE diagnoses and imaging tests and percentage of positive imaging tests based on the 2009 NEDS, stratified by age and sex. Parenthetical percentages represent percentage of total ED visits.

Modeling flow-diverter stents with image-based CFD

Vitaliy L. Rayz[1], Gabriel Acevedo-Bolton[1], Van Halbach[2], Alastair J. Martin[1] and David Saloner[1]
[1]Radiology, UCSF, [2]Neurointerventional Radiology, UCSF.

Introduction. Intracranial aneurysms unsuited for clipping or coiling may be treated by flow-diverting stents (FDS). The fine struts of the FDS create some resistance to the flow across the stent's wall, thus reducing the flow into the aneurismal sac and causing its thrombotic occlusion. In this study computational fluid dynamics (CFD) models based on preoperative MRA/MRI were used to predict postoperative flows in 3 intracranial aneurysms considered for FDS treatment.

Methods. CE-MRA images of 3 ICA aneurysms were used to generate patient-specific geometries. Computations of the preoperative and postoperative flow were carried out with FLUENT. To simulate the postoperative flow, the FDS was modeled as a thin porous tube. In one case, a silicone flow phantom of the aneurysmal ICA was constructed and the UCSF neuro-interventional team deployed an FDS in this model. The postoperative flow in the phantom was measured with 4D MRI velocimetry (4D MRV) and compared to CFD predictions.

Results. For Patient 1, the preoperative flow fields measured in vivo with 4D MRV and computed with CFD are shown in Fig.1 (a) and (b). In each approach the results showed a jet extending across the aneurysm and two counter-rotating vortices. The flow following the FDS deployment measured with 4D MRV in a stented phantom is shown in panel (c) and postoperative CFD results are shown in panel (d). The high-velocity jet through the aneurysm is eliminated as the flow is diverted by the FDS into the distal ICA. There is very good qualitative agreement between CFD predictions of post-procedural flow and the 4D MRV data.

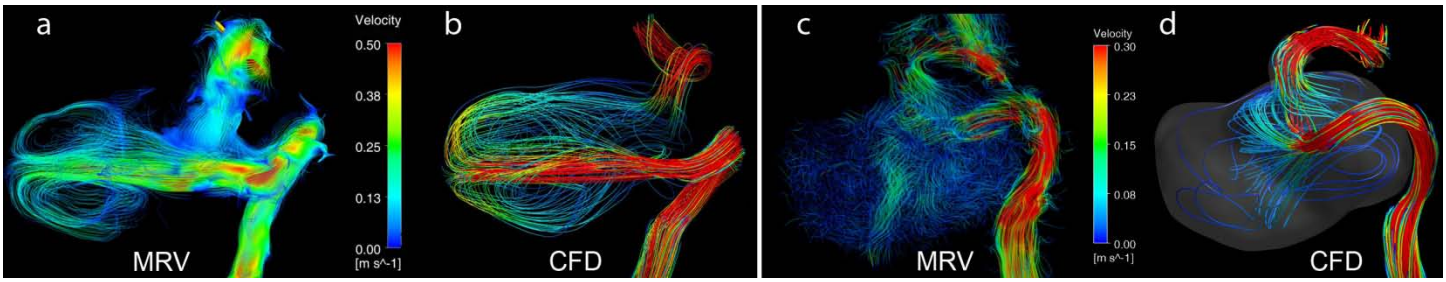

Figure 1 *Patient 1: Preoperative streamlines obtained with (a) in vivo PC-MRI, (b) CFD. Postoperative streamlines obtained with (c) in vitro PC-MRI, (d) CFD.*

For Patient 2, a comparison of the preoperative flow measured in vivo with 4D MRI (Fig 2.a) and computed with CFD (Fig 2.b) shows a remarkable similarity. The CFD-predicted flow following an FDS placement is shown in Fig 2 (c). Most of the flow follows the stent geometry, however there is still some flow leaking through the proximal part of the FDS model.

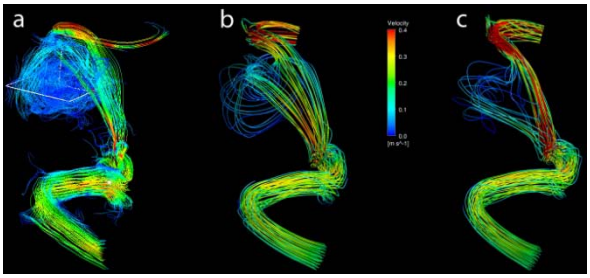

Figure 2 *Patient 2: Preoperative streamlines obtained with (a) in vivo 4D MRV, (b) CFD. Postoperative streamlines predicted with CFD (c).*

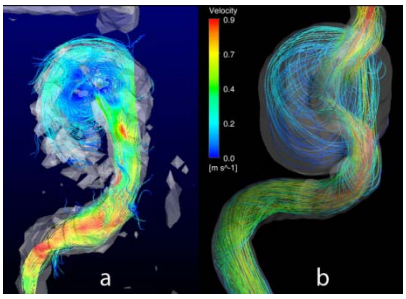

For patient 3, the flow following an FDS placement was acquired in vivo with 4D MRV and compared to CFD predictions (Fig 3). Both methods show that substantial fraction of flow leaks through the FDS, creating a vortex in the aneurysmal sac. Nevertheless, the procedure succeeded in reducing the flow velocities in the aneurysm.

Figure 3 *Patient 3: Postoperative streamlines (a) measured in vivo with 4D MRV, (b) predicted with CFD.*

Conclusions. The results indicate that CFD models constructed from MRI data can be used to predict the efficacy of FDS's and help in evaluating this therapy on a patient-specific basis.

Acknowledgments: This study is supported by NIH Grant NS059891

Robust Image Registration for *in vivo* human osteoarthritic knees and cartilage specimens using T1ρ Magnetic Resonance Imaging Relaxation Times

Wei-Ching Lo[1], Subburaj Karupppasamy[1], Sharmila Majumdar[1], Michael Ries[2], Xiaojuan Li[1]
[1]Department of Radiology and Biomedical Imaging, University of California, San Francisco, San Francisco, CA.
[2]Department of Orthopaedic Surgery, University of California, San Francisco, San Francisco, CA.

Background: Modern developments in cartilage grafting and tissue engineering have increased the demand for the detection of macromolecular changes in osteoarthritic cartilage *in vivo* and *ex vivo* [1]. Quantitative MRI T1ρ relaxation times have been developed to detect early biochemical changes in cartilage matrix. Previous studies correlated quantitative MRI T1ρ relaxation times with biochemical changes within cartilage matrix using specimens taken from total knee arthroplasty [2], but no study has yet documented the relationship between *in vivo* and *ex vivo* T1ρ quantification in cartilage. The purposes of this study are to develop an image registration algorithm for evaluation of the correlation between *in vivo* and *ex vivo* human osteoarthritic cartilages using T1ρ relaxation time.

Materials and Methods: Eight patients (five women; mean age: 68 ± 9 years) who were going to undergo total knee arthroplasty (TKA) due to severe OA were scanned before TKA surgery. The knee specimens were then resected and scanned *ex vivo*, with the specimens being positioned in the corresponding physiological orientation [2]. All scans were acquired using a 3T GE Signa MR Scanner with an 8-channel phased-array knee coil. The 3D sagittal high-resolution fat-saturated SPGR images and sagittal T1ρ relaxation time mapping images (MAPSS) [3] were used in this study. T1ρ maps were reconstructed by fitting the T1ρ-weighted images voxel by voxel to the equation: $S(TSL) \propto \exp(-TSL/T1\rho)$. The 2D contours segmented in 3D SPGR images [4] were reconstructed into a 3D model and transferred to appropriate initial position. Surface points of the specimen model were registered to the *in vivo* cartilage by use of an iterative closest point shape-matching algorithm [5] (Fig. 1). The specimen cartilage ROI was overlaid to the registered *in vivo* T1ρ maps. The *ex vivo* and *in vivo* T1ρ were then quantified in the exactly same regions of cartilage respectively.

Results and Discussion: Eleven specimens (2 LT, 4 LIFC, 4 LPFC, and 1 MIFC) were scanned with MRI. The mean T1ρ values of the *ex-vivo* specimens were significantly higher than *in vivo* T1ρ in the same regions (71.1±3.6 ms vs. 41.9±3.8 ms, $p < 0.0001$). The *in vivo* T1ρ relaxation times showed a significant moderate positive correlation with *ex vivo* T1ρ relaxation times (R^2=.45, p<0.0001, Fig. 2).

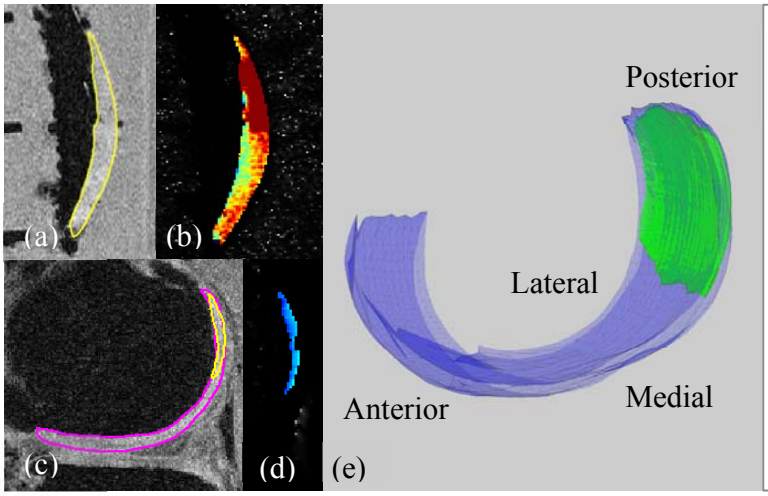

Figure1. Cartilage of specimens (a) and *in-vivo* knees (c) was registered (e) before T1ρ relaxation time quantification (b, d).

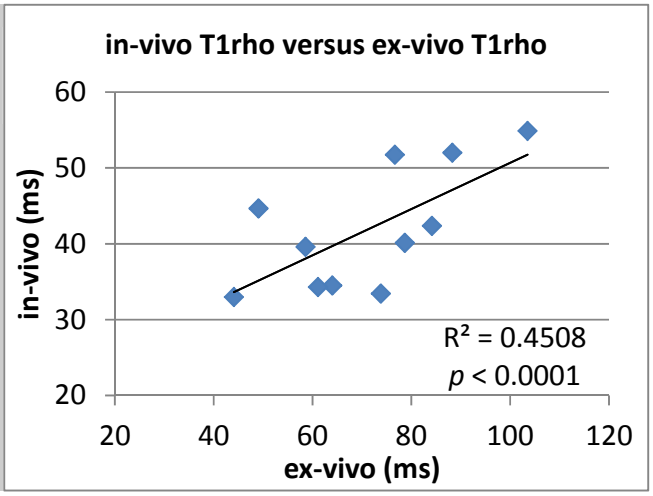

Figure2. Moderate correlation was found between *in-vivo* and *ex-vivo* human osteoarthritic cartilage.

Discussion and Conclusion: This study developed a robust registration algorithm for *in vivo* and *ex vivo* cartilage imaging. The Significant elevation of T1ρ in specimens may be explained by hydration and further degeneration during specimen preparation. The *ex vivo* imaging of specimens are powerful tools to explore the link between imaging measures and biochemical analysis. Ultimately we need to link the biochemical analysis with *in vivo* imaging measures. Thus the registration between *in vivo* and *ex vivo* imaging will be critical to fulfill this goal.

Acknowledgments: The research was supported by K25 AR053633, R01 AR46905, R21 AR056773.

[1] Regatte et al., J Magn Reson Imaging, 2006
[2] Li et al., Magn Reson Imaging, 2011
[3] Li et al., Osteoarthritis Cartilage, 2007
[4] Carballido-Gamio et al., Conf Proc IEEE Eng Med Biol Soc, 2006
[5] Besl et al., IEEE TPAMI, 1992

Geometry, density distribution and internal structure of the proximal femur in relation to age and hip fracture risk in women

J. Carballido-Gamio, R. Harnish, I. Saeed, T. Streeper, S. Sigurdsson, S. Amin, E.J. Atkinson, T.M. Therneau, K. Siggeirsdottir, X. Cheng, L.J. Melton III, J. Keyak, V. Gudnason, S. Khosla, T.B. Harris, T.F. Lang

Age-related changes in hip structure are non-homogeneous. The least mechanically-stimulated regions are thought to experience the greatest bone loss and are implicated in hip fracture because they are thought to bear the bulk of impact from lateral falls. Here we examine how the geometry, distribution of bone mineral density (BMD), and internal structure of the hip vary with age and fracture status using inter-subject image registration, voxel-based morphometry (VBM; Ashburner 2000), and tensor-based morphometry (TBM; Davatzikos 1996). A subset of 349 women representing an age-stratified, random community sample (Riggs 2004) was subdivided into young (<45 yrs; n=94), middle-age (45-59 yrs; n=98), and older (≥60 yrs; n=157) groups (Aging Study). A second subset of 222 age-matched (mean=79.3 yrs) women of the Age, Gene/Environment Susceptibility Reykjavik cohort (Sigurdsson 2006) was subdivided into control (no hip fracture; n=148) and fracture (incident hip fracture; n=74) groups (Fracture Study). Using QCT scans and spatial normalization to minimum deformation templates (MDTs), global differences in bone size, and local differences in BMD (VBM) and volume (TBM) between middle-age and young, older and young, and control and fracture women were identified. Local differences were computed with voxel-wise general linear models yielding Student's t-test statistical maps (T-maps; Figure 1). Weight and height, and age, weight and height were used as covariates in the Aging and Fracture Studies, respectively. For TBM, surface-based analysis (Rajagopalan 2011) and computation of principal deformation directions were also performed (Rajagopalan 2010). Bones of older and fracture women were significantly larger than those of young and control women, respectively. In middle-age and older women, BMD was preserved in the load-bearing inferomedial and inferolateral cortices, but there were BMD deficits superiorly in the femoral neck. Fracture women had lower BMD in expected areas such as the superior cortex and trochanteric region, but differences were also seen in the inferomedial and inferolateral cortices. TBM showed contractions in the principal compressive bands and cortices, and expansions of the trabecular neck area in middle-age and older women compared to young women, and in fracture women compared to age-matched controls. A focal region of cortical volume loss in the superior neck of fracture women was in agreement with a recent study indicating cortical thinning in this area (Johannesdottir 2011). This study shows that women who sustain incident hip fracture have structural differences from age-matched controls and a structural phenotype that is fundamentally distinct from that of normal aging, with BMD deficits in hip regions that are usually preserved with age.

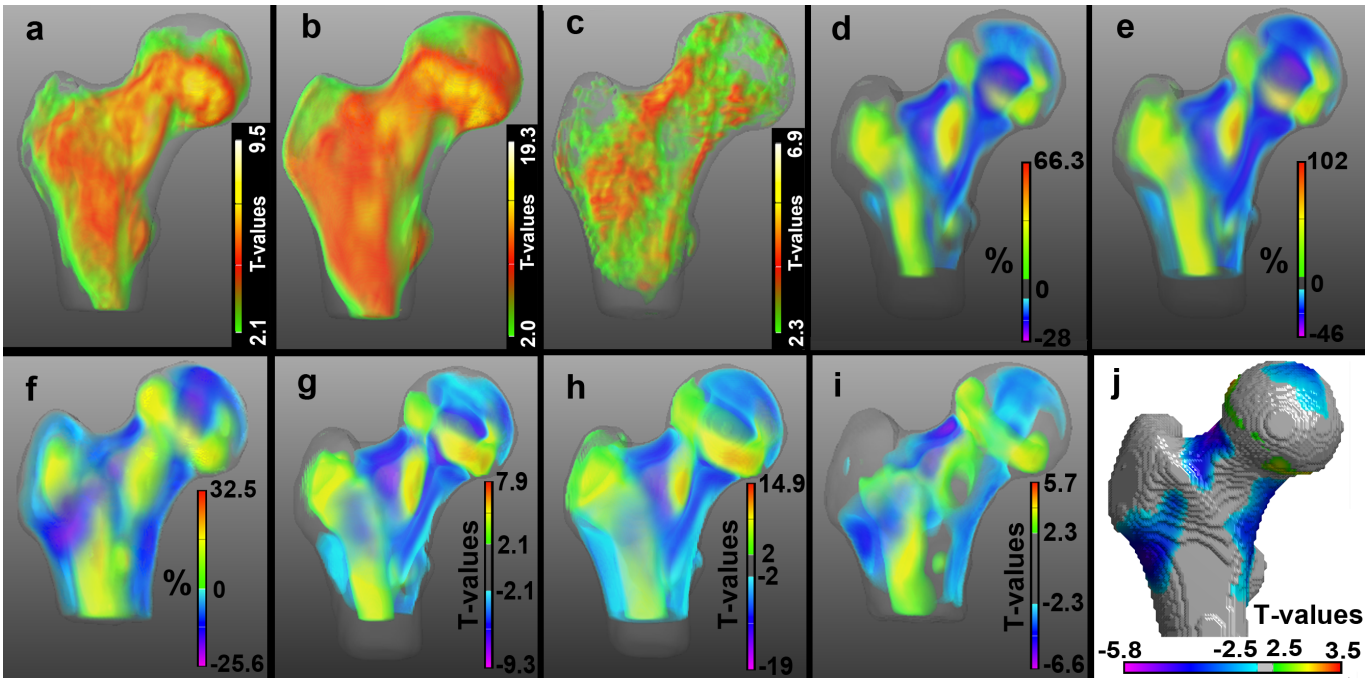

Figure 1. Volumetric representations of VBM T-Maps: a) middle-age vs young; b) older vs young; c) fracture vs controls. Transparency was applied proportionally to T-values. Volumetric representations of local percentage volume differences: d) middle-age vs young; e) older vs young; f) fracture vs controls. Volumetric representations of TBM T-Maps: g) middle-age vs young; h) older vs young; i) fracture vs controls. Transparency was applied proportionally to T-values. Surface TBM T-Map: j) fracture vs controls. Non-significant voxels were rendered gray.

Hyperpolarized ^{13}C MR spectroscopy using [1-^{13}C] dehydroascorbate in a murine model of prostate cancer: comparison with [^{18}F]FDG

Kayvan R. Keshari, Victor Sai, Henry F. VanBrocklin, Zhen J. Wang, John Kurhanewicz, David M. Wilson

Introduction: Reduction and oxidation (redox) chemistry is increasingly implicated in cancer pathogenesis. In order to interrogate the redox status of prostate tumors non-invasively, we developed hyperpolarized [1-^{13}C] dehydroascorbate (HP DHA), the oxidized form of Vitamin C (VitC), as an MR probe[1]. In a transgenic adenocarcinoma of the mouse prostate (TRAMP) model, increased reduction of HP DHA to VitC was observed in tumor, as compared to normal prostate and surrounding benign tissue. We hypothesized that this difference was due to higher concentrations of glutathione (GSH), and increased transport of HP DHA via the glucose transporters (GLUT 1,3,4) in TRAMP tumors. To test these hypotheses, HP ^{13}C MR and positron emission tomography (PET) were employed as complementary technologies in the TRAMP model using HP DHA and [^{18}F] FDG.

Methods: Late-stage TRAMP tumors (>2 cm^3) were studied at similar time-points (MR studies conducted < 24 hours following PET) in fasted mice by FDG-PET and HP ^{13}C MR using HP DHA. MR studies were conducted at 3T using a dual tune ^{1}H/^{13}C volume coil and double spin-echo symmetric echo planar spectroscopic imaging (EPSI) sequence[2]. PET scans were conducted on an Inveon micro PET/CT. PET data were processed using open-source AMIDE software to compare tumor SUVs to those of surrounding tissue[3]. MR data were processed using custom software written in Matlab (Mathworks Inc.) to compare metabolite ratios [VitC]/[DHA + VitC]. Following *in vivo* studies, glutathione was quantified using a spectrophotometric assay and thiol staining was performed using Mercury Orange[4]. Real-time PCR (RT-PCR) and immunohistochemistry were used to evaluate the relevant transporters GLUT1,3,4 and SVCT1,2. Additionally, diffusion-weighted ^{1}H MRI was performed at 14T and apparent diffusion coefficients (ADC) values were calculated for TRAMP tumors and the normal murine prostate.

Results: The average metabolite ratio [VitC]/[DHA + VitC] was 0.28 ± 0.02 in TRAMP tumor, 2.5 fold higher than that of surrounding benign tissue (0.11 ± 0.02, N=4 for both P<0.05). The corresponding tumor/non-tumor FDG uptake ratio was 3 (**Figure**). The total glutathione was 5.1 ± 0.4mM in tumor, and 1.0 ± 0.2mM in normal prostate, while reduced glutathione (GSH) was 2.5 fold higher (2.0 ± 0.3mM v. 0.8 ± 0.3mM, respectively P<0.05). In the TRAMP tumor, mercury orange staining demonstrated increased thiols. RT-PCR showed no significant difference in GLUT1 mRNA with comparable findings in immunohistochemistry staining (anti-GLUT1). ADC values for TRAMP tumors were significantly lower than those calculated for the normal prostate, consistent with increased cellularity.

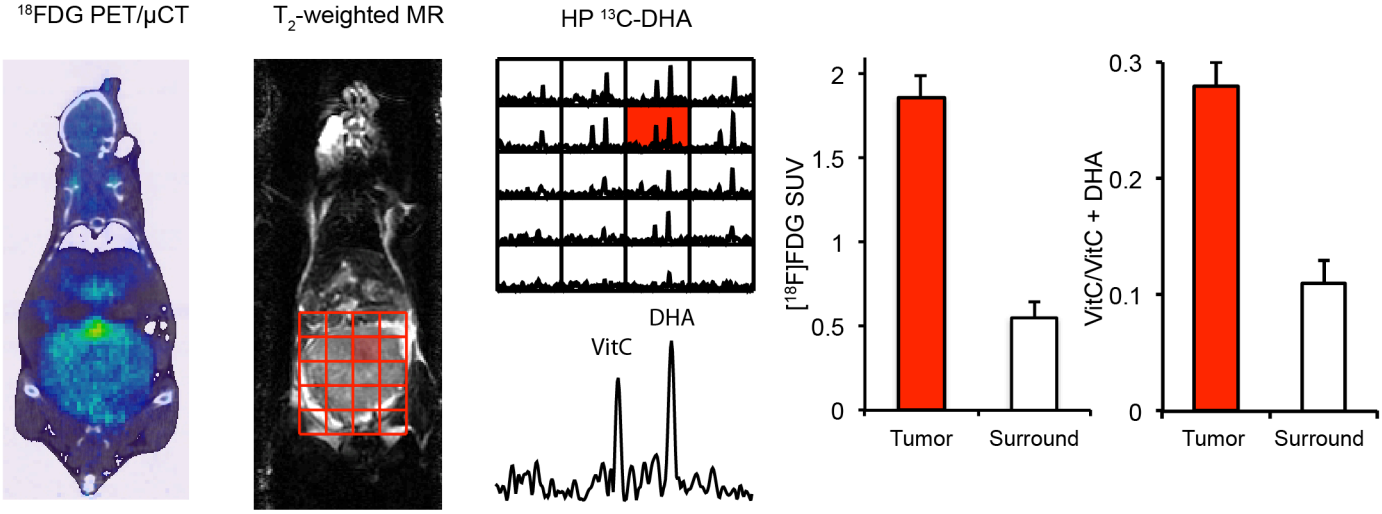

Conclusion: Both HP DHA and FDG provide similar tumor contrast in the TRAMP model. Our findings suggest that the mechanism of in vivo HP DHA reduction and the resulting tumor contrast correlates most strongly with GSH concentration. In the TRAMP model, GLUT1 is not significantly upregulated and unlikely to account for the contrast obtained using HP DHA or FDG.

References: [1] Keshari et al. PNAS 2011 [2] Yen et al. Magn Res Med 2009 [3] Loening et al. Mol Imaging 2003 [4] Vukovic et al. Clin Cancer Res 2000

Quantitative 7T Phase Imaging in Presymptomatic Huntington's Disease

A. C. Apple[1], K. Possin[2], G. Satris[2], J. M. Lupo[1], A. Jakary[1], K. Wong[2], D. A. C. Kelley[3], G. Kang[2], M. Geschwind[2], S. J. Nelson[1], and C. P. Hess[4]

[1]Department of Radiology and Biomedical Imaging, University of California, San Francisco, San Francisco, CA, United States, [2]Department of Neurology, University of California, San Francisco, San Francisco, CA, United States, [3]GE Healthcare, Global Applied Sciences Laboratory

Introduction: Prior postmortem and in vivo MRI studies of Huntington's disease (HD) have demonstrated iron deposition and atrophy within the basal ganglia [1]. Quantitative measurements of local field shift (LFS) derived from phase images are in part related to brain iron concentration [2]. In this work, we exploited the phase sensitivity of ultra-high field 7T MRI to characterize caudate LFS in subjects with genetically confirmed but premanifest HD (preHD) and compared the results to caudate volume, currently the most well accepted imaging marker of disease progression [3].

Methods: Thirteen subjects with genetically confirmed preHD and 11 matched controls were scanned on both 7T and 3T MR scanners (GE Healthcare, Milwaukee, WI) according to a protocol approved by our institutional review board. At 7T, gradient echo images (GRE) were acquired along with volumetric T1-weighted images. At 3T, volumetric T1-weighted imaging was performed for accurate segmentation and morphometry, which was not possible using 7T T1-weighted images due to field inhomogeneity-related variations in image intensity. LFS maps were created from GRE phase images and normalized by the phase of the posterior limb of the internal capsule (PLIC), a non-diseased white matter region of interest (ROI). Caudate ROIs were created with from the 3T T1 and, using an FSL automated tool, were co-registered with the 7T GRE images using FSL[4]; average LFS within the right and left caudate nuclei were derived (Figure 1). For comparison, Freesurfer (MGH Martinos Center for Biomedical Imaging) was used to obtain measurements of normalized caudate volume. Caudate volumes and mean LFS for controls and preHD subjects were compared using the Wilcoxen ranked-sum test.

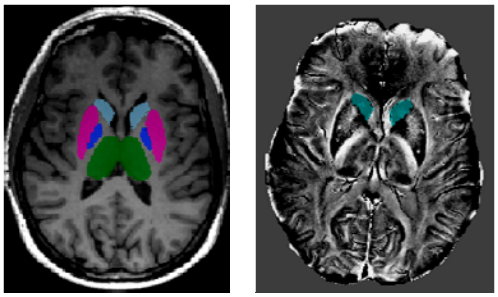

Figure 1. ROIs were extracted with FSL from the 3T T1; the caudate is shown here (cyan). Caudate ROIs were then registered and overlaid on phase images to calculate LFS

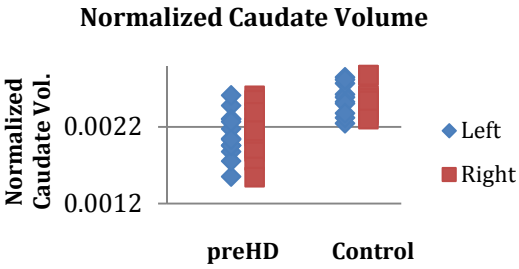

Figure 2. Caudate volumes normalized by total intracranial volume

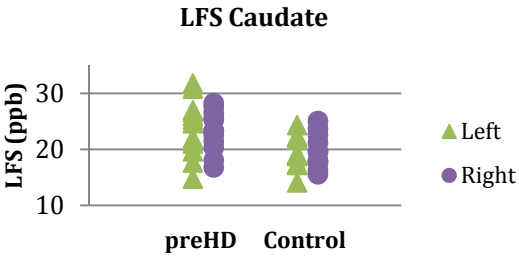

Figure 3. Caudate LFS normalized with the average phase from the PLIC

Results and Discussion: No significant age or gender differences were found between proHD and control groups. Mean ages for patients and controls were 46.46 and 40.91 respectively; the mean number of genetic CAG repeats for HD was 42.72. PreHD patients showed significantly smaller left and right caudate volumes ($P<0.01$) as compared with controls (Figure 2). PreHD subjects showed significantly higher mean right and left caudate LFS compared to controls (Figure 3). LFS represents a composite measure of susceptibility effects, which are related to a number of factors including the presence of iron, calcium, and deoxyhemoglobin within vascular structures. We speculate that differences in caudate LFS in patients with preHD are due to iron deposition and loss of neuronal cytoarchitecture. A direct relationship between caudate volume and LFS was not observed, suggesting that LFS and volume may represent different pathologic endpoints of neurodegeneration.

Conclusions: Currently, the most studied method for evaluating disease progression in HD is volumetric measurement of the caudate. We conclude that quantitative measurement of phase with high field 7T imaging may also represent a useful biomarker for early stage HD.

References: [1] Bartzokis et al. Arch Neurol 1999; 56:569-574 [2] Hammond et al. Neuroimage 2008; 39:1682-1 [3] Weir DW et al. Lancet Neurol 2011; 10: 573-90. [4] M.W. Woolrich, et al.. NeuroImage, 2009 45:S173-186, 2009

Targeting uPAR with Antagonistic Recombinant Human Antibodies in Aggressive Breast Cancer

Aaron M. LeBeau, Sai Duriseti, Charles S. Craik and Henry F. VanBrocklin

Background: The urokinase plasminogen activator receptor (uPAR) is a promising target for the non-invasive imaging and treatment of breast cancers with aggressive phenotypes. mRNA analysis of patients from the Netherlands Cancer Institute (NKI) dataset found that uPAR expression was highest in the basal-like breast cancer (BLBC) subtype which exhibits a triple-negative phenotype (absence of the Her2, estrogen receptor, and progesterone receptor). Triple-negative breast cancer (TNBC) is an extremely aggressive form of cancer that predominantly affects young premenopausal women. Effective treatment options for TNBC currently do not exist and the disease free survival is the shortest of any breast cancer. The development of new treatments for TNBC is greatly hampered by the in ability to effectively gauge therapeutic response in a majority of patients. New imaging agents are urgently needed to evaluate therapeutic response in TNBC patients. Detailed here is the development of novel uPAR-targeted human antibody probes that can be radiolabeled for imaging and radioimmunotherapy (RIT) in preclinical TNBC models.

Methods: Human antibodies specific for uPAR were discovered using a human Fab phage display library. The IgG antibodies were labeled with near-IR fluorophores for optical imaging and with ^{111}In for SPECT imaging in MDA-MB-231 orthotopic xenografts. Mice given an intracardiac injection of MDA-MB-231 cells (dissemination model) were used to evaluate the sensitivity of ^{111}In-IgG for micrometastasis detection compared to ^{18}F- FDG-PET. An RIT study using ^{177}Lu-IgG was performed in MDA-MB-231 orthotopic xenografts. The 150 µCi dose was fractionated two weeks apart over the course of a five week study to decrease toxicity.

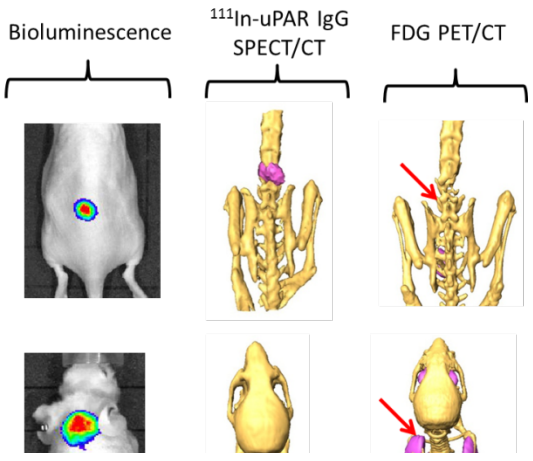

Imaging metastatic TNBC lesions in an MDA-MB-231 intracardiac dissemination model. MDA-MB-231 lesions that stably express luciferase were imaged with bioluminescence imaging (BLI). ^{111}In-labeled uPAR antibodies co-localized to the BLI signal while the clinical standard, FDG-PET, did not. Inflammation was detected by FDG-PET in one mouse (lower right).

Results: In MDA-MB-231 xenografts, fluorophore and ^{111}In-IgG antibodies demonstrated specific probe localization to the tumors using optical and SPECT imaging. ^{111}In-IgG successfully imaged the tumors in the dissemination model and were found to be superior to ^{18}F-FDG at detecting both osseous and soft-tissue metastases. At day 35 of the RIT study, animals treated with the ^{177}Lu-IgG had tumors volumes of 50 ± 43 mm^3, while the saline control had volumes of 1166 ± 201 mm^3.

Conclusions: Human antibodies that target uPAR in TNBC preclinical models have been prepared and selected. The SPECT probes were found to be more accurate and sensitive than ^{18}F- FDG at detecting metastatic lesions in mice. When radiolabeled with ^{177}Lu, the probes were effective RIT agents. These agents may be useful for evaluating and treating TNBC

Unique Morphology of the Brain Reward/Executive Oversight System and the Relation to Cognition and Impulsivity in Polysubstance Abusers

D.L. Pennington; T.C. Durazzo; T. Schmidt; C. Abe; A. Mon; D.J. Meyerhoff

Center for Imaging of Neurodegenerative Diseases, San Francisco VA Medical Center, Department of Radiology and Biomedical Imaging, University of California, San Francisco
San Francisco, CA 94121

BACKGROUND: The clinical reality in treatment centers today is at least 50% of patients present with combinations of alcohol use disorders (AUD) and various substance use disorders. The brain reward/executive oversight system (BREOS) is implicated in the development and maintenance of all addictive disorders. Assessment of the integrity of BREOS components and its relationship to cognitive functioning is critical for a better understanding of the mechanisms of relapse in these polysubstance users (PSU).

METHODS: Treatment seeking PSU (n=30, abstinent for 30 ± 8 days) and AUD (n=30, abstinent 33 ± 9 days) individuals along with non-smoking light drinking controls (NSLD, n=30) completed 4T brain magnetic resonance imaging studies. Groups were compared on parcellated morphological data obtained with FreeSurfer methodology for the following bilateral components of the BREOS and their sub-regions: dorsolateral prefrontal (DPFC), anterior cingulate (ACC), orbitofrontal cortex (OFC), and insula. Additionally, morphological comparisons were also made between future PSU abstainers or relapsers based on their relapse status at 3 months or beyond. PSU were also assessed on 11 traditional domains of cognition. A sub-sample of this population also received the following measures of self-regulation: Balloon Analogue Risk Task (BART), Barratt Impulsiveness Scale (BIS), Iowa Gambling Task (IGT). PSU BREOS and their sub-regions were correlated with the traditional cognitive and self-regulation measures.

RESULTS: PSU showed thinner cortices and smaller volume in the OFC compared to LD. Both PSU and AUD had thinner insula than LD. BREOS cortical thickness was similar in PSU and AUD, but OFC cortical volume tended to be smaller in PSU. Thicker ACC and OFC sub-regional cortices predicted relapse in PSU. Within the PSU, greater BREOS volume was related to better overall cognitive function and better performance in 6 of 11 cognitive domains. Larger DLPFC and OFC volumes in the PSU tended to be related to lower non planning impulsivity, while thicker cortices of the BREOS were related to lower levels of attentional and total impulsivity. Unexpectedly, thicker BREOS cortices related to poorer performance in auditory-verbal learning/memory, and larger BREOS, DLPFC, and OFC volumes were related to increased risk taking.

CONCLUSIONS: BREOS morphometry differentiate PSU from both AUD and LD. The OFC and other BREOS sub-regions may be sensitive to morphological abnormalities specific to PSU and may serve as neurobiological markers of PSU relapse. Within the PSU, greater BREOS volume is associated with better cognition and impulse control but not risk taking. The unexpected findings illustrate that PSU are not only different from AUD, but they suggest different relationships between morphology and function that are modulated by factors not considered in this analysis. Our findings warrant further analyses and the inclusion of longitudinal study designs to broaden our understanding and help tailor treatment to the specific deficits exhibited by this highly understudied but large population of substance abusers.